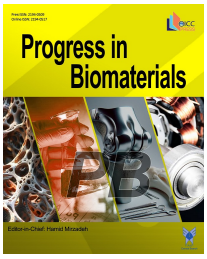

Prog. Biomater. 2026; 15(1) : 45-61

Progress in Biomaterials (PIBM)

https://doi.org/10.57647/pibm.2026.152606

Research Article

Engineering Biocompatible and Bioactive Poly (glycerol sebacate)-Based Scaffolds Reinforced with Polypyrrole-Functionalized Nanocellulose for Neural Tissue Regeneration

Sayeh Drakhshan Fakhr[1], Salar Mohammadi Shabestari[2], Arshia Akbari Jafroudi[1], Narges Dadeshzadeh[1], Mohammad Hossin Allahyari[1], Shahrokh Shojaei[1,3,*], Pedram Tehrani[1], Vahabodin Goodarzi[4,*]

[1]*Department of Biomedical Engineering, CT.C., Islamic Azad University, Tehran, Iran*
[2]*Department of Polymer, School of Chemical Engineering, College of Engineering, University of Tehran, Tehran, Iran*
[3]*Stem Cells Research Center, Tissue Engineering and Regenerative Medicine Institute, Central Tehran Branch, Islamic Azad University, Tehran, Iran*
[4]*Tissue Engineering and Regenerative Medicine Research Center, Baqiyatallah University of Medical Sciences, Tehran, Iran*

*__Corresponding authors:__ shahrokh.shojaei@gmail.com, and v.goodarzi@hotmail.com

Article History

Received:
29 August 2025

Revised:
20 February 2026

Accepted:
24 February 2026

Published in Issue:
31 March 2026

Abstract:

In this study, biocompatible and mechanically tunable composite scaffolds were developed using poly (glycerol sebacate) (PGS), polycaprolactone (PCL), and polypyrrole-functionalized cellulose nanofibers (Ppy-CNFs) for neural tissue engineering. To enhance elasticity and strength, 30 wt.% PCL was incorporated into PGS, while 0.5% and 1% CNFs were introduced to improve conductivity, bioactivity, and structural stability. FTIR confirmed successful HDI crosslinking and chemical compatibility among the components. XRD showed increased crystallinity with PCL and peak broadening with CNFs, indicating nanofiber dispersion. Thermal analysis (TGA/DTG) revealed enhanced stability, with the main degradation peak shifting from 405 °C in pure PGS to 425 °C in PGS/PCL/CNFs composites, accompanied by higher char yield due to PPy shielding effects. Mechanical tests demonstrated marked improvements, with compressive strength increasing from 7.12 MPa to 24.62 MPa and Young's modulus from 1.83 MPa to 5.76 MPa. Contact angle measurements rose from 62.3° to 73.7°, maintaining favorable hydrophilicity for cell interactions. SEM revealed uniformly porous surfaces and well-dispersed nanofibers. Biological studies confirmed excellent cytocompatibility, with SH-SY5Y cell viability increasing from 84.94% to 91.09%. Enhanced spreading, neurite anchoring, and nuclear integrity were observed, highlighting the multifunctional properties of the optimized scaffold for neural tissue regeneration.

Keywords: Poly (glycerol sebacate) scaffold; Polypyrrole-functionalized cellulose nanofiber; Neural tissue engineering; Thermo-mechanical characterization; Cell viability and adhesion

Cite this article: Drakhshan Fakhr S, Mohammadi Shabestari S, Akbari Jafroudi A, Dadeshzadeh N, Allahyari MH, Shojaei Sh, Tehrani P, Goodarzi V. Engineering Biocompatible and Bioactive Poly (glycerol sebacate)-Based Scaffolds Reinforced with Polypyrrole-Functionalized Nanocellulose for Neural Tissue Regeneration. Prog. Biomater. 2026;15(1), 45-61. https://doi.org/10.57647/pibm.2026.152606

1. Introduction

In recent decades, neural tissue engineering (NTE) has emerged as a promising multidisciplinary strategy to address the complex challenge of regenerating injured or degenerated nervous tissues, particularly in the central and peripheral nervous systems (CNS and PNS)

[1]. Damage to neural tissues can result from trauma, ischemia, neurodegenerative disorders, or malignant conditions such as glioblastoma, leading to permanent functional impairments due to the limited regenerative capacity of the CNS and the inadequate outcomes of current clinical treatments [2, 3]. Although autografts and allografts have traditionally been employed for peripheral nerve repair, they present significant limitations, including donor site morbidity, immunogenic reactions, and inconsistent regeneration outcomes [4]. Consequently, the development of bioengineered scaffolds that mimic the native extracellular matrix (ECM) and support cellular attachment, proliferation, differentiation, and guided axonal growth has become a focal point of research in regenerative medicine [5]. Beyond structural regeneration, emerging therapeutic strategies have highlighted the importance of modulating the neural microenvironment through anti-inflammatory and regenerative signaling pathways to improve functional recovery following neural injury [6, 7].

A key component in successful NTE strategies is the design of three-dimensional (3D) scaffolds with physicochemical, mechanical, and biological properties that closely replicate the neural microenvironment. These scaffolds not only provide a physical substrate for cell anchorage and migration but also serve as bioactive platforms that influence cell behavior through topographical, mechanical, and biochemical cues. The selection of scaffold materials is crucial, as it determines the scaffold's biocompatibility, biodegradability, mechanical integrity, and ability to integrate with host tissues [8, 9].

Among various classes of biomaterials, synthetic and natural polymers have gained substantial interest in scaffold fabrication. Synthetic polymers such as polycaprolactone (PCL), polylactic acid (PLA), and poly (lactic-co-glycolic acid) (PLGA) offer tunable mechanical properties, ease of processing, and controlled degradation rates. However, they often lack cell recognition sites and may require surface modification or blending with bioactive components to enhance cellular interactions [10]. On the other hand, natural polymers like collagen, gelatin, hyaluronic acid, and cellulose exhibit excellent biocompatibility and inherent biological activity but typically suffer from poor mechanical strength and fast degradation [11].

To overcome these limitations, recent studies have focused on hybrid polymer-based systems that combine the advantages of both synthetic and natural polymers, not only in scaffold design but also in multifunctional nanomaterial platforms for biomedical applications [12, 13]. In this context, poly (glycerol sebacate) (PGS), a biocompatible and elastomeric polyester synthesized via polycondensation of glycerol and sebacic acid, has garnered attention for its flexibility, favorable degradation profile, and cytocompatibility [14]. PGS closely mimics the mechanical behavior of soft tissues and has shown promise in neural applications. Its degradation products are non-toxic and can be resorbed by physiological processes [15]. Moreover, the synthesis of PGS allows for tunable mechanical and degradation properties by varying the reaction time, temperature, and molar ratio of monomers, making it an excellent candidate for soft tissue regeneration. Nonetheless, its mechanical strength and long-term stability remain insufficient for certain load-bearing or extended regeneration applications [16].

To reinforce the structural integrity of PGS-based scaffolds, blending with PCL has been proposed. PCL, an FDA-approved, semi-crystalline aliphatic polyester, provides long-term mechanical support, slow biodegradation, and processability through diverse fabrication techniques [17]. PCL enhances the mechanical robustness and modulates the degradation kinetics of hybrid scaffolds, enabling better control over scaffold performance during the regenerative process [18]. Importantly, the PGS-PCL composite system can be fine-tuned to achieve a desirable balance between elasticity and rigidity, which is particularly important in nerve tissue applications where mechanical mismatch can impair integration and function [19].

However, neither PGS nor PCL inherently possesses electrical conductivity, which is a vital property in neural tissue engineering due to the electrosensitive nature of neurons. Electrical cues play a crucial role in neural signaling and regeneration [20]. Conductive biomaterials that can transmit electrical stimuli to cells are known to enhance neurite outgrowth, synapse formation, and overall neurogenesis. Consequently, incorporating electrically conductive components into scaffold formulations has become a central design consideration [21]. One of the most promising strategies involves the integration of conductive polymers such as polypyrrole (PPy), which exhibits excellent electrical conductivity, environmental stability, and proven biocompatibility. PPy, when appropriately synthesized and deposited, can endow otherwise non-conductive scaffolds with electroactive functionality without significantly compromising their cytocompatibility [22].

Despite the advantages of PPy, its inherent brittleness and poor mechanical integrity make it unsuitable for standalone scaffold fabrication. Therefore, it is commonly used as a surface coating or in combination with supportive polymers to impart conductivity [23]. In our approach, PPy was not utilized only for its conductive properties but also to modify cellulose nanofibers (CNFs), thereby improving both the electrical characteristics and surface functionality of the nanofibers. CNFs, derived from waste paper through environmentally friendly processing, offer a sustainable, renewable, and cost-effective solution for scaffold reinforcement. These nanofibers provide excellent mechanical strength, high aspect ratio, and tunable surface chemistry, making them ideal candidates for reinforcing polymer matrices [24].

The functionalization of CNFs with PPy significantly enhances their electroactivity while maintaining their biocompatibility and structural properties. This dual modification transforms CNFs into multifunctional reinforcements capable of improving the scaffold's overall performance. The resulting PPy-CNFs nanostructures

https://doi.org/10.57647/pibm.2026.152606

integrate mechanical reinforcement, surface roughness, hydrophilicity, and electrical conductivity-critical parameters that collectively influence neural cell behavior.

In this study, we aimed to design and fabricate a novel 3D nanocomposite scaffold composed of PGS and PCL integrated with PPy-CNFs using a salt-leaching method. This scaffold was engineered to exhibit optimized porosity, biocompatibility, and mechanical and electrical properties tailored for neural tissue regeneration. The PGS matrix served as the elastomeric base to mimic the neural tissue's compliance, while PCL enhanced structural stability and sustained degradation. PPy-CNFs served a dual role as a mechanical reinforcer and an electroactive element to support neuron-specific cellular behaviors.

To fabricate the scaffolds, a multi-phase synthesis approach integrating bio-based and conductive components was employed. The final 3D structure was developed using a salt leaching technique, a well-established method for generating interconnected porosity within polymeric matrices. In this strategy, porogens such as salt particles are uniformly dispersed within the polymer blend and subsequently removed through aqueous leaching, leaving behind a porous architecture. This method enables precise control over pore size and distribution by tuning the salt particle size and concentration, making it particularly suitable for tissue engineering applications requiring high permeability and cell infiltration [25, 26].

To ensure the suitability of the developed scaffolds for neural tissue engineering, a comprehensive set of characterization techniques was considered essential for evaluating their physicochemical, morphological, thermal, mechanical, and biological attributes. Spectroscopic, microscopic, and thermal analyses were utilized to verify the successful integration of composite components, the formation of interconnected porous networks, and the thermal integrity of the scaffolds. Additionally, wettability and mechanical assessments were employed to examine surface properties and load-bearing capacity, both critical factors for cell adhesion and structural stability *in vivo*. Finally, *in vitro* biological evaluations using neural model cells were included to assess cytocompatibility and the scaffold's potential to support neural cell proliferation and attachment. Therefore, scaffold biocompatibility in this study is evaluated through a combination of *in vitro* cellular assays and physicochemical characterizations that are known to influence cell–material interactions.

This integrated approach underscores the potential of multifunctional nanocomposite scaffolds as advanced platforms for neural tissue engineering. By synergistically combining the elasticity of PGS, the mechanical stability of PCL, and the conductive and bioactive features of PPy-CNFs, the developed scaffold addresses multiple design criteria required for effective nerve regeneration. Unlike many existing neural scaffolds that prioritize either biocompatibility, mechanical stability, or electrical functionality, the present study aims to integrate these features within a single elastomeric composite platform [27, 28]. This study not only contributes to the current knowledge of scaffold-based neural repair but also provides a sustainable and translational strategy for future applications in regenerative medicine, particularly in personalized nerve grafts and bioelectronic interfaces.

2. Materials and method

2.1 Materials

Sebacic acid and glycerol were purchased from Merck. Polycaprolactone and Sodium chloride were obtained from Sigma-Aldrich. Hexamethylene diisocyanate and 1,4-dioxane were also acquired from Merck. Polypyrrole was sourced from Merck. Dimethyl sulfoxide was obtained from Merck. Deionized water was provided by Zolal (Iran), and phosphate-buffered saline was purchased from DNAbiotech. SH-SY5Y human neuroblastoma cells were obtained from the Iranian National Cell Bank. DMEM, fetal bovine serum, penicillin-streptomycin, and trypsin-EDTA were all purchased from Gibco. MTT and DAPI stains were supplied by Sigma.

2.2 Method to synthesis smples

Cellulose nanofibers were extracted from waste paper soaked in water and mechanically shredded. The pulp was treated with NaOH to remove residual impurities. Subsequently, phosphoric acid was added to introduce phosphate functional groups, and the resulting fibers were dried and ground into powder. PPy was polymerized in situ on the CNFs surface in the presence of an oxidizing agent to obtain electroactive PPy-CNFs. The modified nanofibers were stored in a dry environment before blending. PGS prepolymer was synthesized by reacting sebacic acid and glycerol at a 1:1 molar ratio in a vacuum reactor at 120 °C for 6 h. The resulting resin was then mixed with PCL (70:30 ratio) in a binary solvent system of dioxane and DMSO. HDI and tin octoate were added to initiate crosslinking and ensure network stability. Following PGS/PCL blending, NCe was incorporated at 0.5% and 1% w/w to obtain composite formulations. NaCl was added as porogen, and the mixtures were cast into cylindrical molds. Samples were left to dry at room temperature. Salt leaching was performed using deionized water for 48 h with periodic water changes. The scaffolds were then vacuum-dried until complete solvent and salt removal.

The fabricated scaffolds included four formulations: S1 (PGS), S2 (PGS/PCL 70:30), S3 (PGS/PCL/0.5% PPy-CNFs), and S4 (PGS/PCL/1% PPy-CNFs). The schematic of the synthesis steps is presented in Scheme 1.

2.3 Characterization

The physicochemical, structural, surface, mechanical, and biological properties of the fabricated scaffolds were evaluated using the following techniques: Fourier-transform infrared spectroscopy (FTIR) was performed using a Tensor II spectrometer (Bruker, Germany) in the range of 400 – 4000 cm^{-1} to analyze the chemical functional groups and confirm the presence of specific bonds related to scaffold components. Morphological anal-

https://doi.org/10.57647/pibm.2026.152606

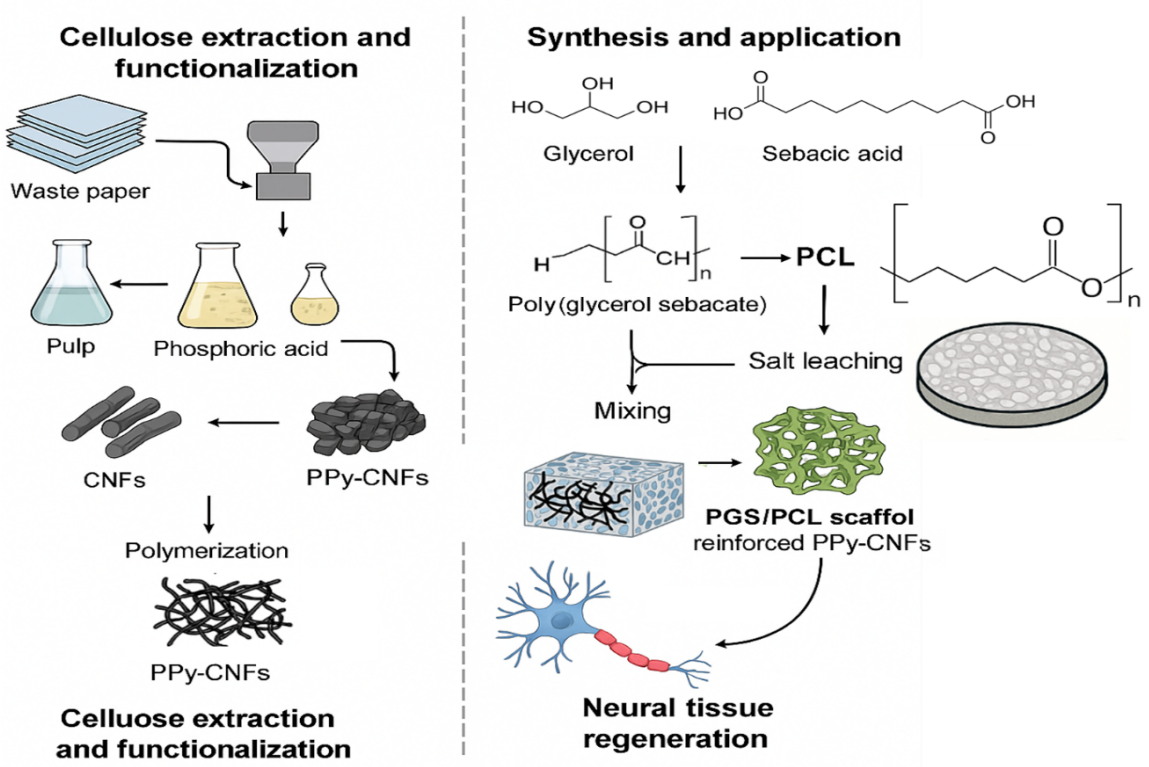

Scheme 1. Schematic overview of PPy- CNFs preparation and integration into PGS/PCL scaffolds via salt leaching for neural tissue engineering.

ysis was carried out by scanning electron microscopy (SEM) using a TESCAN Vega microscope. Prior to imaging, samples were sputter-coated with a thin layer of gold using a Q150R ES coating system to enhance conductivity. X-ray diffraction (XRD) was conducted using a D8 ADVANCE diffractometer (Bruker, Germany) equipped with Cu Kα radiation (λ = 1.54 Å) and a Ni filter. Data were collected in the 2θ range of $10 - 80°$ with a step size of 0.02° and 1 s dwell time to evaluate the crystalline structure and phase composition. Contact angle measurements were performed using a CAG-20 goniometer to assess the wettability of the scaffold surface. A 5 µL water droplet was placed on the surface of samples (5 × 5 cm), and the static contact angle was recorded using high-resolution image capture and analyzed with digital processing software. Thermal stability of the scaffolds was analyzed by thermogravimetric analysis (TGA) under a nitrogen atmosphere from 25 °C to 600 °C, evaluating degradation profiles of composite components. Mechanical properties were evaluated using uniaxial compression tests on cylindrical scaffolds. Compressive strength and Young's modulus were calculated from stress-strain curves to assess the structural integrity and elasticity of the scaffolds. Mechanical properties were evaluated by uniaxial compression testing, and stress–strain data were used to calculate Young's modulus and compressive strength. Cell viability was assessed by MTT assay. For this, scaffolds were incubated in culture media for 24 h, and 5000 SH-SY5Y cells were seeded in the scaffold-conditioned media and cultured for an additional 24 h. MTT reagent (5 mg/mL in PBS, diluted 1:10) was added at 100 µL per well and incubated for $3 - 4$ h at 37 °C. The metabolically active cells reduced the yellow tetrazolium salt (MTT) to insoluble purple formazan crystals. After removing the supernatant, 100 µL of DMSO was added to each well to dissolve the crystals, and the absorbance was measured at 570 nm using a microplate reader.

The percentage of viable cells was calculated using the following equation [29]:

$$\text{Cell viability}(\%) = \frac{OD_e - OD_b}{OD_c - OD_b} \times 100 \qquad (1)$$

In this equation, OD_e, OD_c, and OD_b correspond respectively to the absorption peak intensity at 570 nanometers for cell-containing scaffolds, control samples, and empty plates. Following 24-hour incubation, scaffolds seeded with SH-SY5Y cells were fixed using 4% paraformaldehyde (w/v) in PBS for 20 minutes at room temperature. After washing with PBS, cells were permeabilized with 0.3% Triton X-100 in PBS for 10 minutes to enable intracellular access. To block nonspecific antibody binding, samples were incubated in 10% (v/v) goat serum for 1 hour at room temperature. Subsequently, scaffolds were incubated with the appropriate primary antibody diluted in blocking buffer overnight at 4 °C. After three washes with PBS, secondary antibody conjugated with a fluorescent dye was applied and incubated for 90 minutes at 37 °C in the dark to prevent photobleaching. Nuclear staining was carried out using 4′,6-diamidino-2-phenylindole (DAPI, 1 µg/mL in PBS) for 10 minutes at room temperature. Finally, samples were mounted and imaged using a fluorescence microscope (Olympus, Tokyo, Japan) equipped

https://doi.org/10.57647/pibm.2026.152606

with DAPI-specific filters. All staining procedures were performed under sterile and light-protected conditions. All quantitative data were analyzed using SPSS software (version 20). Normality of distribution was verified, and statistical significance was determined using one-way ANOVA followed by Tukey's post hoc test. A p-value less than 0.05 was considered statistically significant. All quantitative results were expressed as mean ± SD based on at least three independent replicates ($n \geq 3$). SD reflects the degree of dispersion and reproducibility of measurements, providing an estimate of the consistency across samples within each experimental group. Data analysis and SD calculation were performed using SPSS version 20 (IBM Corp., USA) and visualized using OriginPro 2023.

3. Result and discussion

3.1 Structural characterization by FTIR and XRD

Figure 1 presents the FTIR spectra used to confirm the chemical structure and interactions among the scaffold components. In Fig. 1 (a), the characteristic spectra of the pure precursors-glycerol, sebacic acid, and pre-PGS-are displayed. Glycerol exhibits a broad O–H stretching band at 3200−3600 cm^{-1} and notable bending vibrations of hydroxyl groups between 1400–1500 cm^{-1} [30, 31]. Sebacic acid shows C–H stretching in the 2800 – 3000 cm^{-1} region and a strong carbonyl (C=O) peak around 1700 cm^{-1} [32]. The pre-PGS spectrum demonstrates the successful polycondensation of glycerol and sebacic acid, evidenced by the emergence of ester carbonyl (C=O) stretching around 1730 cm^{-1} and C–O–C stretching in the range of 1100 – 1300 cm^{-1} [17]. Simultaneously, the intensities of O–H and COOH bands are reduced, indicating their conversion to ester linkages [33].

In Fig. 1 (b), the FTIR spectra of the synthesized scaffolds (S1 to S4) are presented. All formulations show a broad band at 3200 – 3400 cm^{-1}, corresponding to O–H and N–H stretching vibrations originating from residual hydroxyls and PPy incorporation, respectively [34]. The peaks observed at 2850 – 2950 cm^{-1} and around 1450 cm^{-1} are attributed to CH_2 symmetric and asymmetric stretching and bending, common to both PGS and PCL. The ester C=O stretching band at 1730 cm^{-1} increases in intensity with the addition of PCL and CNFs (S3 and S4), indicating enhanced ester content and higher molecular ordering due to crosslinking. Furthermore, aromatic C=C stretching peaks between 1500 – 1600 cm^{-1} confirm the presence of PPy in the composite matrix [35]. In the fingerprint region, notable differences in peak intensity and position between samples indicate intermolecular interactions between PGS/PCL and the functionalized CNFs.

Collectively, Fig. 1 (a) confirms the successful synthesis of the prepolymer, while Fig. 1 (b) verifies the integration of all composite constituents and highlights chemical compatibility and network formation in the scaffold system.

XRD analysis was conducted to investigate the crystalline behavior of scaffolds S1 through S4. As shown in figure 2, all samples exhibit a broad diffraction peak centered around $2\theta = 20.04°$, which is characteristic of semi-crystalline polymeric systems. This pattern reflects a predominance of amorphous regions with limited molecular ordering, typical for elastomeric matrices such as PGS and the blended PGS/PCL systems.

In sample S1 (PGS), the broad peak reflects its inherent low crystallinity and rubber-like behavior [19]. With the introduction of PCL in S2, the overall diffraction intensity slightly decreases, likely due to increased molecular entanglement and phase mixing that disrupts PGS crystallinity, despite PCL itself being a semi-crystalline polymer [36]. This reduction may be attributed to kinetic hindrance during scaffold solidification and the interference of PCL chains with ordered PGS domains [37].

Samples S3 and S4, which incorporate 0.5% and 1% PPy-CNFs respectively, show a modest increase in peak intensity at the same angle without the formation of sharp

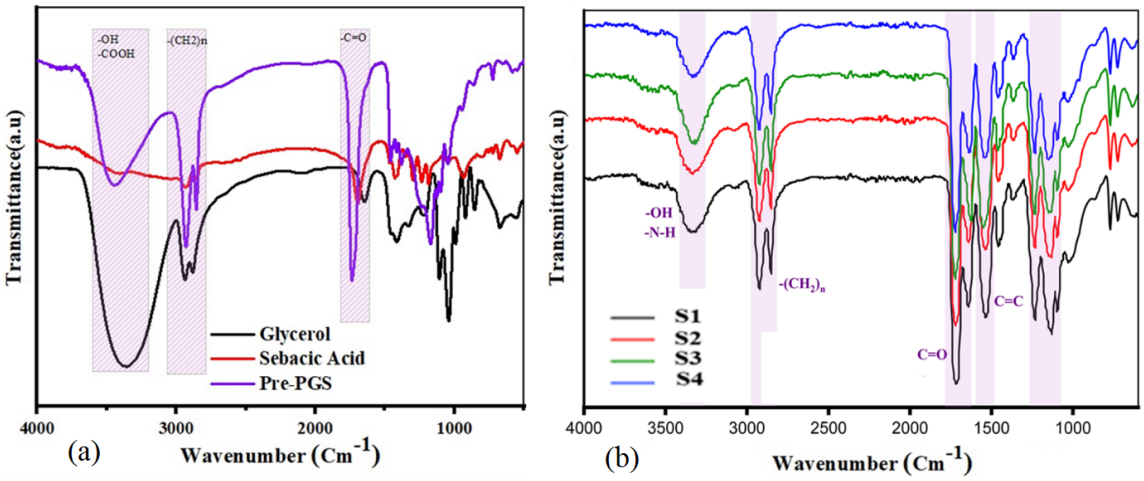

Figure 1. FTIR spectra of raw materials and fabricated scaffolds. (a) FTIR spectra of glycerol, sebacic acid, and pre-PGS, er bond formation during pre-polymer synthesis. (b) FTIR spectra of scaffolds S1–S4, showing characteristic absorption bands associated with PGS, PCL, and PPy-functionalized nanocellulose, indicating successful incorporation of all components without the formation of undesirable chemical byproducts.

https://doi.org/10.57647/pibm.2026.152606

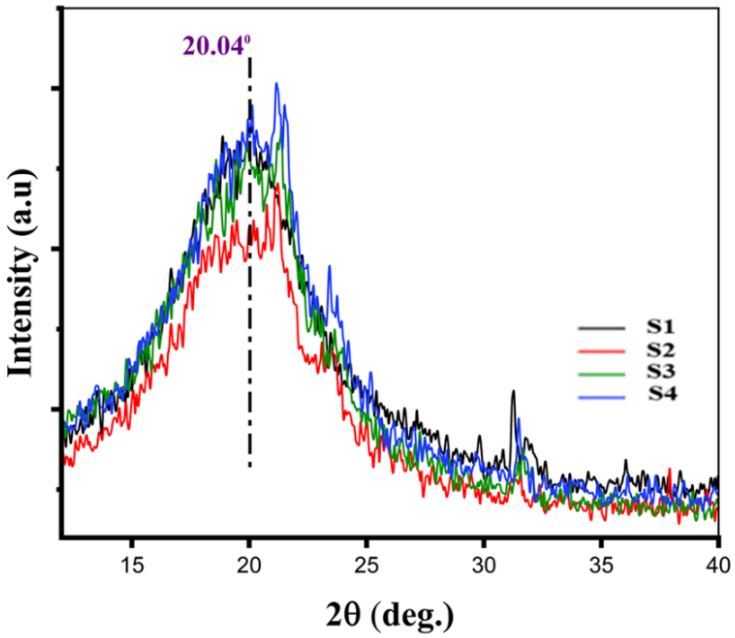

Figure 2. XRD patterns of scaffolds S1–S4. The diffraction profiles reveal the semi-crystalline nature of the PGS/PCL-based scaffolds, while the absence of sharp additional peaks associated with nanocellulose or PPy suggests good dispersion of the reinforcing phase within the polymer matrix.

new peaks. This behavior suggests improved molecular alignment or local ordering induced by the presence of the conductive nanofibers. While the cellulose backbone is largely amorphous, its surface modification with polypyrrole enhances interaction with the surrounding matrix, potentially serving as nucleation points that promote semi-crystalline phase formation [38].

The absence of secondary peaks confirms that no distinct crystalline phase from the nanofibers dominates the diffraction profile, implying good dispersion and physical compatibility. Overall, the XRD data supports the hypothesis that the conductive nanofibers reinforce the scaffold microstructure by enhancing local order without altering the amorphous-dominant character of the polymeric matrix.

3.2 Microstructure analysis

The surface morphology and internal architecture of scaffolds were examined using SEM at magnifications of 50 µm, 100 µm, and 500 µm. As illustrated in figure 3 (S1, panels A–C), the PGS scaffold exhibits a well-defined and interconnected porous structure with relatively uniform pore distribution. The pore walls appear smooth and continuous, indicating successful salt-leaching and polymer curing. The presence of interconnected porosity is essential for facilitating nutrient and oxygen transport, cell migration, and vascularization in tissue engineering applications.

In contrast, figure 3 (S2, panels A–C) shows the morphology of the PGS/PCL scaffold. The inclusion of PCL leads to noticeable changes in surface texture and pore architecture. The pore walls appear thicker and less regular compared to S1, and the internal surfaces are rougher, likely due to the hydrophobic nature and slower degradation profile of PCL [39]. These morphological changes are indicative of phase separation between the hydrophilic PGS and hydrophobic PCL, which can modulate the scaffold's degradation rate and mechanical integrity [40]. Moreover, the smaller average pore size observed in S2 may influence cellular infiltration and tissue integration.

As illustrated in figure 4 (S3, panels A–C), the incorporation of nanofibers introduces noticeable surface roughness and structural reinforcement. In panels A and B, nanofiber aggregates are evident on the pore walls (red arrows), suggesting effective physical interaction and partial dispersion within the polymeric matrix. The interconnected porous network remains intact, and the overall pore architecture maintains suitable dimensions for tissue ingrowth.

In figure 4 (S4, panels A–C), increasing the nanofiber content to 1% leads to a more compact and continuous surface morphology. The pore walls appear denser and smoother, and nanofibers are less distinctly aggregated, indicating better distribution. Notably, a three-dimensional interconnected network is still preserved, as seen in the wide-field image (panel C). This structural enhancement is likely due to increased interfacial bonding between the nanofibers and the PGS/PCL matrix, which can improve both mechanical stability and potential cellular response [41].

Overall, the SEM images of S3 and S4 confirm that increasing the content of conductive nanofibers modulates pore surface characteristics and reinforces microstructural integrity without compromising porosity. These features are essential for scaffolds designed for neural tissue engineering, where both electrical conductivity and structural support are critical.

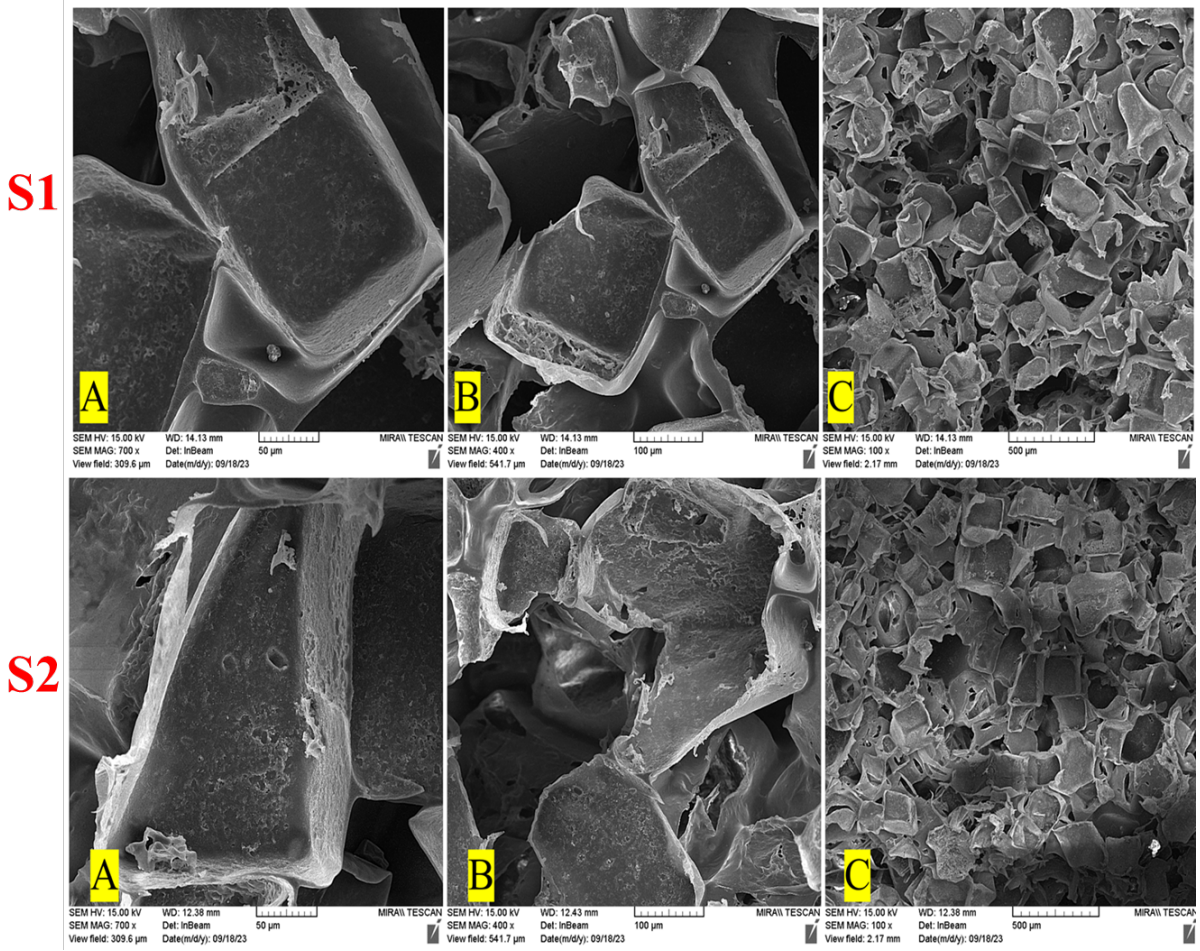

Figure 3. SEM micrographs of scaffold morphologies: (S1, top row: A–C) corresponds to the PGS scaffold, and (S2, bottom row: A–C) corresponds to the PGS/PCL scaffold.

3.3 Thermal analyses

TGA was employed to investigate the thermal stability and decomposition behavior of scaffolds S1 to S4. As shown in Fig. 5 (a), the TGA curves reveal multi-phase degradation patterns, with distinct onset temperatures and degradation slopes for each formulation.

For S1, the degradation profile shows a gradual weight loss starting around 280 °C, followed by a steep decomposition step beginning at 360 – 380 °C, culminating near 430 °C. This behavior suggests a predominantly single-step degradation, with minor pre-decomposition attributable to small fractions of low-molecular-weight oligomers or incompletely crosslinked segments. Therefore, although the curve shows curvature before the main drop, it lacks a well-defined intermediate plateau typically associated with true multi-step decomposition [42].

In contrast, S2 exhibits an earlier and more differentiated thermal profile. The initial decomposition begins at a lower temperature (300 °C), which can be attributed to the thermal instability of PCL, known to degrade in the range of 300–380 °C. This step is followed by a secondary, broader weight loss occurring between 390 – 450 °C, likely corresponding to the breakdown of the PGS network [43]. The two-step behavior is clearly more defined in S2 than in S1.

Samples S3 and S4, containing 0.5% and 1% PPy-CNFs respectively, display enhanced thermal resistance. Their degradation onset shifts toward higher temperatures, and the residual weight after 500 °C increases slightly, indicating improved char formation and enhanced thermal barrier effects. The nanofibers, particularly due to the conjugated structure of polypyrrole, likely restrict thermal motion and enhance matrix integrity, delaying polymer chain scission [44].

The DTG curves in Fig. 5 (b) provide deeper insight into decomposition dynamics. S1 exhibits two thermal decomposition peaks: a less prominent shoulder around 315 °C (Tmax1) likely related to unreacted oligomers or partial crosslinking, and a dominant peak at 405 °C (Tmax2), corresponding to the main degradation of the crosslinked PGS network [45]. In contrast, S2 displays two distinct peaks-a first peak near 335 °C (Tmax1) related to PCL decomposition and a second at 410 °C (Tmax2) linked to PGS. S3 and S4 also exhibit two-step degradation behavior, but with both peaks shifted to higher temperatures (345 °C and 425 °C), indicating that the conductive nanofibers increase thermal stability by altering the degradation kinetics and improving thermal shielding [46].

In addition to molecular rigidity provided by the PPy

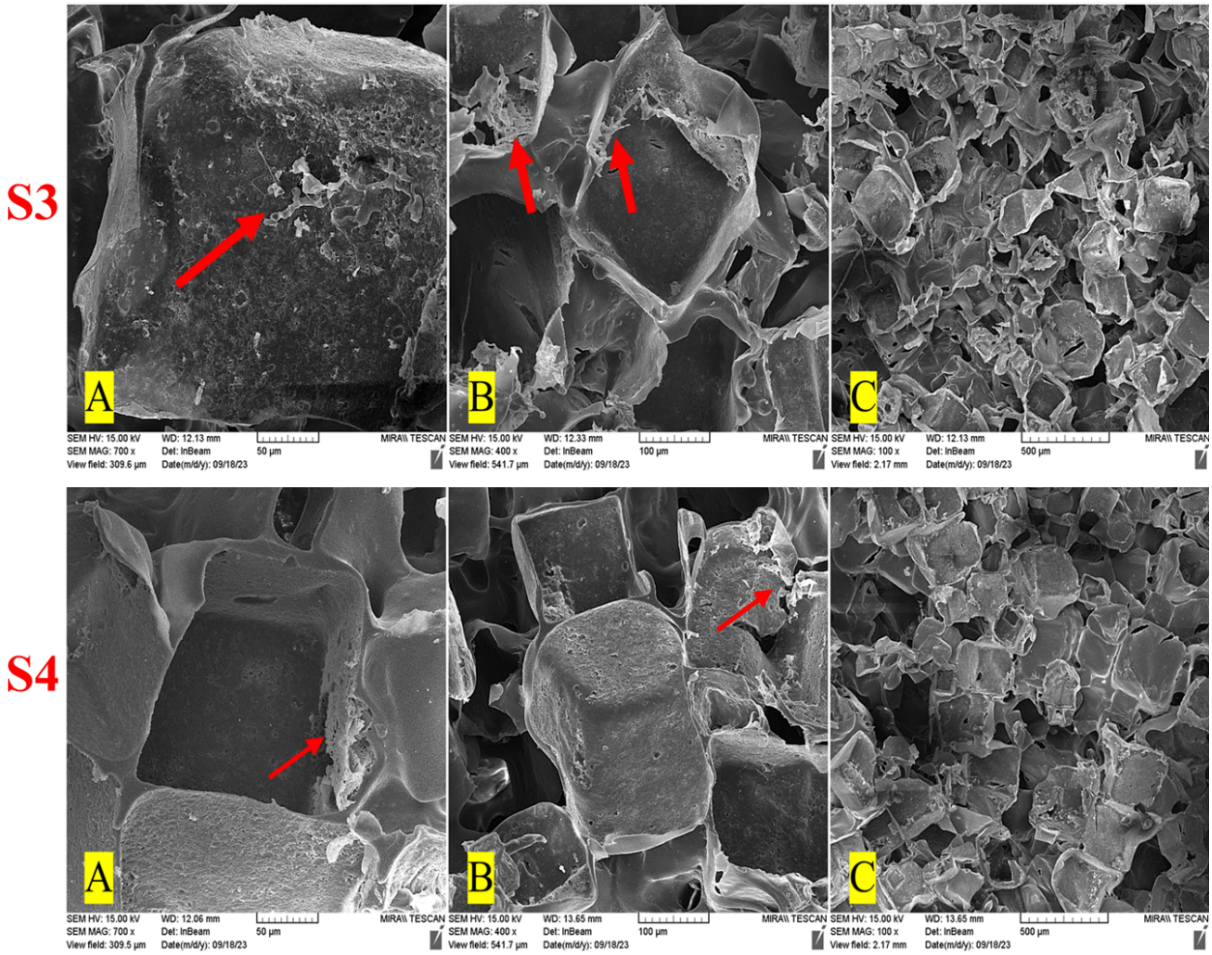

Figure 4. SEM micrographs of scaffolds: S3 A–C (top row) , and S4 A–C (bottom row).

structure, the nanocomposite nature of S3 and S4 contributes to a thermal barrier effect. The well-dispersed nanofibers reduce thermal diffusivity across the matrix, leading to delayed heat penetration and more gradual thermal decomposition. Furthermore, the increased carbonaceous residue observed at high temperatures reflects the improved oxidative resistance and char-forming ability of the nanocomposite scaffolds, which is advantageous for enhancing structural integrity under elevated thermal stress.

3.4 Mechanical analyses

Mechanical properties play a pivotal role in scaffold design for neural tissue engineering, where elasticity, strength, and structural resilience are essential to sup-

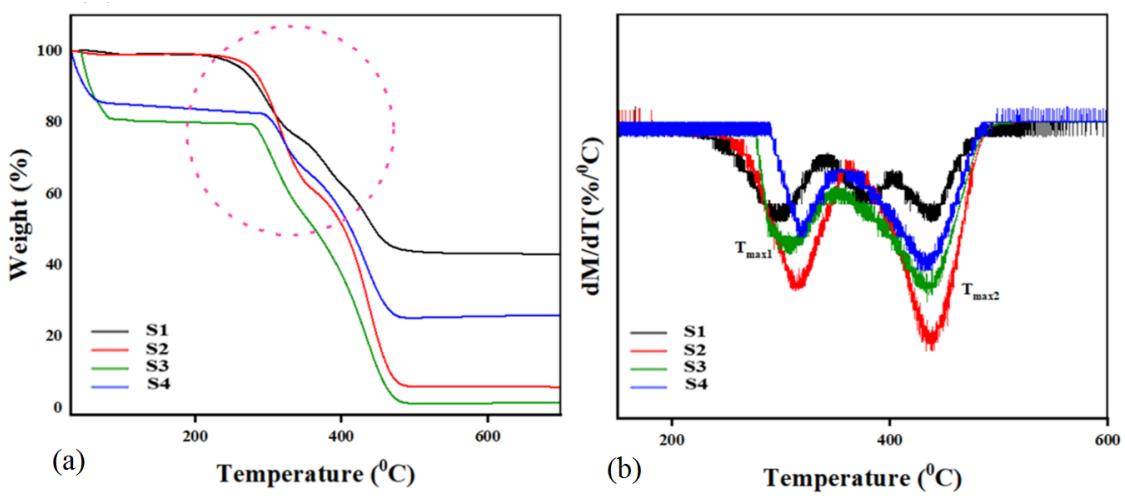

Figure 5. TGA (a) and DTG (b) curves of scaffolds S1–S4 showing distinct thermal degradation profiles.

https://doi.org/10.57647/pibm.2026.152606

port delicate neuronal networks. Figure 6 presents the stress–strain curves of scaffolds S1 to S4, revealing clear differences in elastic modulus, compressive strength, and deformation capacity. Figure 6 shows representative stress–strain curves for each scaffold formulation, while quantitative mechanical parameters were calculated from replicate measurements as described in the Characterization section. Uniaxial compressive mechanical testing was performed to quantitatively evaluate scaffold mechanics. Young's modulus was calculated from the initial linear elastic region of the stress–strain curves, and compressive strength was determined as the maximum stress prior to failure. In this study, structural integrity is reflected by the scaffold's ability to maintain pore architecture and mechanical cohesion under compressive loading.

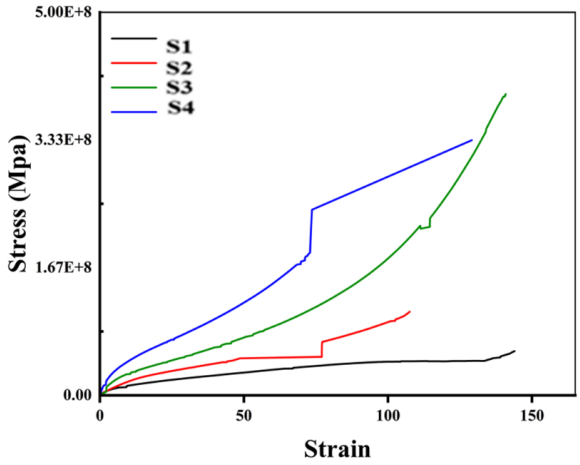

Figure 6. Representative compressive stress–strain curves of scaffolds S1–S4 obtained from uniaxial compression testing. Quantitative mechanical parameters, including Young's modulus and compressive strength, were calculated from replicate measurements ($n \geq 3$) and are reported as mean ± SD, while the plotted curves illustrate representative mechanical behavior. The reported ranges reflect the variability observed among independent specimens.

S1 exhibited the lowest mechanical performance among all formulations, with a shallow slope and extended strain range before failure. The Young's modulus of this scaffold was estimated between 2 – 10 MPa, while the compressive strength remained low due to the highly flexible and amorphous structure of PGS. This elastomeric character allows significant deformation under load but limits load-bearing capacity, making it unsuitable alone for applications requiring mechanical support [47].

In S2, the introduction of 30 wt.% PCL led to a noticeable increase in Young's modulus (1 – 10 MPa) and compressive strength (5 – 20 MPa). This improvement is attributed to the semi-crystalline nature of PCL, which contributes reinforcing domains within the matrix and increases molecular packing density. As a result, this scaffold exhibited higher stiffness and lower elastic deformation, improving dimensional stability and load tolerance [48]. These features make the blend more favorable for neural scaffolding, where moderate mechanical strength is essential to prevent tissue ollapse without inducing excessive rigidity. S3 showed further enhancement in mechanical response, with Young's modulus increasing to the range of 2 – 12 MPa and compressive strength reaching 7 – 25 MPa. The inclusion of 0.5% PPy-CNFs improved structural reinforcement by forming a semi-percolated fiber network that facilitated more efficient stress distribution. This nanofiber-mediated reinforcement plays a critical role in preserving scaffold structural integrity by limiting pore wall deformation and preventing premature collapse under load. PPy -CNFs also promoted interfacial adhesion, improving load transfer and suppressing early failure [49]. While deformation under load was still present, it was reduced compared to S1 and S2. S4 demonstrated the highest mechanical performance, exhibiting the steepest stress–strain slope, the highest compressive modulus, and minimal deformation. Its Young's modulus exceeded 12 MPa, and compressive strength reached above 25 MPa, highlighting the synergistic reinforcement effect of well-dispersed nanofibers at this concentration. The denser nanofiber network and improved fiber–matrix interactions effectively limited polymer chain mobility, increased scaffold cohesion, and reduced structural collapse under load [50]. Importantly, despite the increased stiffness, the scaffold retained sufficient flexibility, maintaining compatibility with soft tissue biomechanics. Collectively, these results confirm that both PCL incorporation and CNFs reinforcement significantly improve scaffold mechanics. The incorporation of nanocellulose fibers significantly enhances scaffold structural integrity by reinforcing the load-bearing framework, improving stress distribution, and maintaining pore architecture during compressive deformation. The mechanical behavior follows a clear trend:
S4 > S3 > S2 > S1, reflecting progressive enhancements in modulus and strength while balancing elasticity and stiffness. This tunability in mechanical properties positions the developed composites, especially S4, as promising candidates for neural tissue engineering applications where structural support and compliance must be delicately balanced.

Overall, uniaxial compression testing provided a quantitative basis for comparing scaffold mechanics, demonstrating a clear and reproducible enhancement in modulus and strength with PCL incorporation and PPy-CNFs reinforcement. Also, Young's modulus increased from 1.83 MPa for S1 to 5.76 MPa for S4, while compressive strength improved from 7.12 MPa to 24.62 MPa, demonstrating the reinforcing effect of PCL and PPy-CNFs.

3.5 Contact angle

Contact angle analysis was conducted to assess the surface wettability of scaffolds S1 through S4, a crucial parameter in neural tissue engineering as it influences protein adsorption, cell adhesion, and subsequent biological responses. The contact angles were measured at 0, 15, 30, 45, and 60 seconds and the values extracted from calibrated imaging software are reported in Table 1 and figure 7.

S1 demonstrated an initial contact angle of 62.3°, with minimal fluctuation over time (final value at 60 seconds: 62.0°), reflecting its inherently hydrophobic character. This behavior is attributed to its smooth, amorphous, and non-polar surface chemistry, which lacks functional groups capable of promoting hydrogen bonding or polar interactions with water molecules [51]. S2 exhibited a slightly lower initial contact angle (58.7°), but the value progressively increased to 64.9° at 60 seconds. The increase in contact angle over time suggests that the presence of semi-crystalline PCL domains may introduce localized surface heterogeneity that temporarily resists water spreading [52]. Although PCL provides additional carbonyl groups, its crystallinity and limited chain mobility at the surface may hinder rapid water absorption [53]. In contrast, S3 showed a more substantial rise in contact angle, starting from 69.3° and reaching 82.8° after 60 seconds. The incorporation of PPy- CNFs was expected to improve hydrophilicity due to the presence of hydroxyl and polar heterocyclic moieties [49]. However, the opposite trend may be explained by a Cassie–Baxter wetting regime, in which nanoscale surface roughness introduced by the nanofiber's traps air pockets under the droplet, increasing the apparent contact angle despite the presence of hydrophilic chemical groups [54]. Additionally, partial aggregation of nanofibers or incomplete exposure of polar moieties at the surface could reduce their wetting efficacy [55]. S4 followed a similar trend with an initial angle of 71.5°, slightly increasing to 73.7° at 60 seconds. Although the increase is less pronounced than in S3, the higher initial value compared to S1 and S2 indicates that nanofiber addition does alter surface morphology. However, the relatively stable trend over time suggests improved nanofiber dispersion in S4, which may minimize surface energy fluctuations and stabilize wettability behavior. Comparatively, the data show that S1 < S2 < S4 < S3 in terms of final contact angle, indicating increasing hydrophobicity across the series. This finding contrasts with typical expectations but highlights the complex interplay of chemical functionality, surface energy, and microscale topology introduced by both PCL and nanofibers. The results emphasize that enhancing wettability in polymeric scaffolds not only depends on chemical composition but also requires control over surface morphology and nanofiber alignment.

3.6 *In vitro* cell analyzes

The cytocompatibility of scaffolds S1 through S4 was evaluated using the MTT assay on SH-SY5Y human neuroblastoma cells after 24 hours of indirect exposure. As

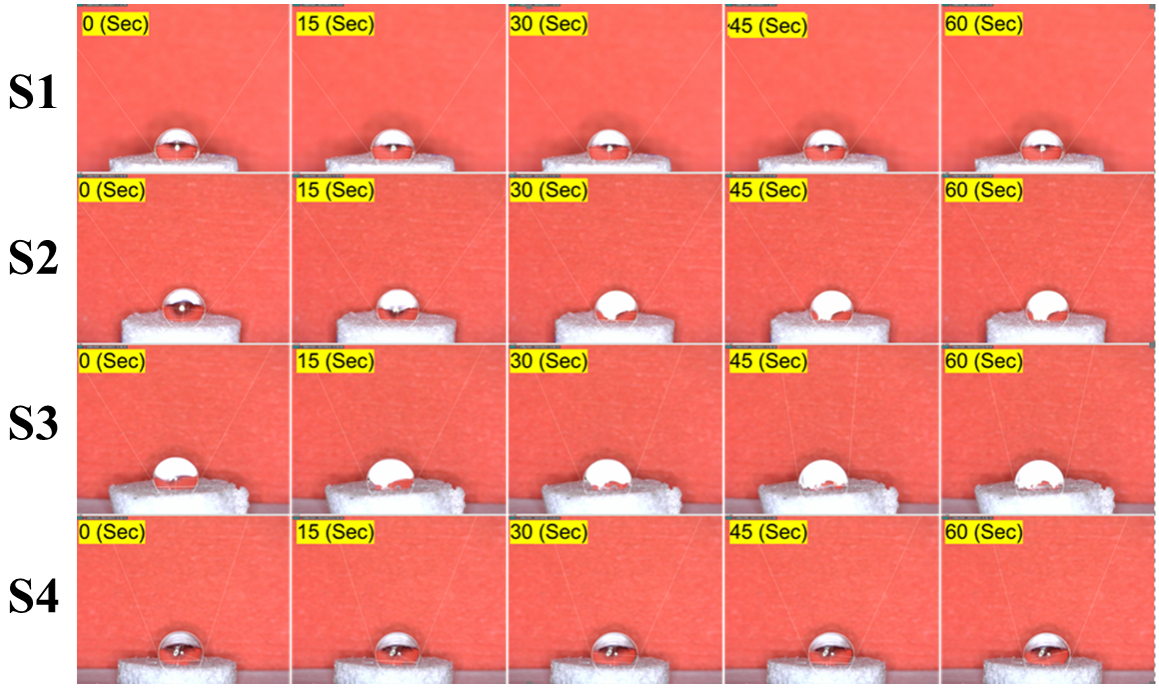

Figure 7. Contact angle images of scaffolds S1–S4 at various time points (0–60 s), showing dynamic changes in surface wettability.

Table 1. Static water contact angle measurements of scaffolds S1–S4 at different time intervals (0–60 s).

Sample	0 s	15 s	30 s	45 s	60 s
S1	62.3	60	60.5	63.9	62.0
S2	58.7	60.1	64.6	64.0	64.9
S3	69.3	73.6	76.7	86.0	82.8
S4	71.5	71.2	72.3	70.1	73.7

https://doi.org/10.57647/pibm.2026.152606

illustrated in figure 8, all tested samples-maintained cell viability above the critical threshold of 70%, confirming their non-cytotoxic nature.

The untreated control group exhibited 100% cell viability. Upon exposure to the PGS scaffold (S1), cell viability decreased to 84.94%, suggesting moderate biocompatibility potentially influenced by acidic degradation by-products released from sebacic acid units. PGS, being a soft elastomer with hydrolyzable ester bonds, can generate local acidification in the microenvironment, which temporarily impacts mitochondrial metabolic activity [56].

Incorporation of PCL in S2 improved cell viability to 90.16%, indicating enhanced biocompatibility. This improvement is likely attributed to the semi-crystalline and hydrophobic nature of PCL, which reduces the hydrolysis rate and stabilizes the scaffold surface, thereby minimizing pH fluctuations and cellular stress [57].

Further enhancement was observed in the nanocomposite scaffolds. S3, containing 0.5% PPy- CNFs, demonstrated 88.93% viability, while S4, with 1% PPy- CNFs, exhibited the highest viability of 91.09%. The incorporation of PPy- CNFs improves scaffold surface roughness and provides bioactive cues that promote cell attachment [58]. Moreover, the mild conductivity introduced by PPy can enhance neural cell–material interaction and favor cytoskeletal organization, contributing to improved cell viability [59].

Overall, all scaffolds exhibited non-cytotoxic profiles with increasing cell viability in the order: S1 < S3 < S2 < S4, highlighting the synergistic benefits of PCL and CNFs incorporation in tuning scaffold biointerface and enhancing neural cell compatibility.

To further assess the cell–scaffold interactions, SEM imaging and DAPI staining were selectively performed on S1 and S4 scaffolds, representing the lowest and highest cell viability, respectively. As the viability percentages of S2 and S3 were relatively close and did not exhibit statistically significant differences, including them in subsequent morphological and nuclear evaluations was considered redundant. This comparative strategy enabled a focused analysis of cellular behavior across the two extremes of scaffold performance, providing clearer insights into the impact of scaffold composition on neural cell compatibility.

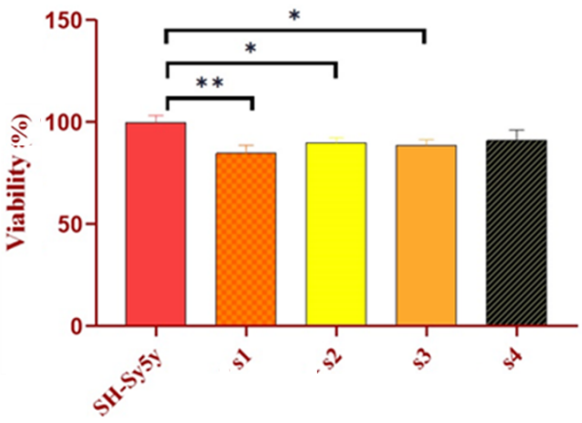

Figure 8. MTT assay results of SH-SY5Y cells after 24-hour exposure to scaffolds S1–S4. Cell viability is presented as percentage relative to the untreated control group (SH-SY5Y). All scaffold groups exhibited acceptable biocompatibility, with a significant decrease in viability observed in S1 compared to the control ($p < 0.01$) and moderate significance relative to S2 and S4 ($p < 0.05$). Data are expressed as mean ± standard deviation ($n = 3$). Statistical significance: $^{*}p < 0.05$, $^{*}p < 0.01$.

To assess the scaffold–cell interface and adhesion behavior, SEM images were obtained after culturing SH-SY5Y cells on scaffolds S1 and S4. The results are presented in figure 9, showing significant morphological differences in cell attachment between the two formulations.

In the PGS scaffold (S1), cells appear sparsely distributed with minimal surface interaction. The cell morphology remains mostly rounded with limited pseudopod extension, indicating weak attachment and poor cytoskeletal anchorage. This may be attributed to the relatively smooth and hydrophobic surface of pure PGS, along with its low mechanical stiffness, which limits integrin-mediated cell engagement and focal adhesion formation [60].

In contrast, the S4 scaffold, containing PCL and 1% PPy- CNFs, exhibited dense cellular attachment and widespread coverage of the scaffold surface. The adhered cells displayed well-spread morphologies, with visible filopodia and lamellipodia bridging the scaffold pores. This improved adhesion is likely due to multiple synergistic factors: the presence of PCL enhances mechanical integrity and surface heterogeneity, while the PPy- CNFs increase roughness, protein adsorption capacity, and surface energy [35, 61]. These properties promote cytoskeletal organization and integrin clustering, critical for sustained neural cell adhesion and signaling.

Overall, the comparative images confirm that incorporation of both PCL and conductive nanofibers significantly enhances cell–scaffold interactions. The observed differences underscore the importance of surface topography, biochemical cues, and mechanical compatibility in designing scaffolds optimized for neural tissue engineering.

To further evaluate the adhesion and distribution of SH-SY5Y neuroblastoma cells on the scaffolds, DAPI staining was performed after 24 hours of culture. As shown in figure 10, nuclei appear as distinct blue fluorescent spots, allowing visualization of the density and spatial distribution of attached cells on both S1 and S4 surfaces.

In the S1 group, a relatively lower density of nuclei is observed across the imaged fields, suggesting reduced cell attachment and spreading. This observation aligns with previous SEM findings and is likely due to the limited bioactivity, smooth morphology, and lack of specific nanoscale surface features in pure PGS. Additionally, the low mechanical stiffness of PGS restricts cytoskeletal tension development, impeding proper focal adhesion formation.

Conversely, scaffold S4 exhibited a substantially

https://doi.org/10.57647/pibm.2026.152606

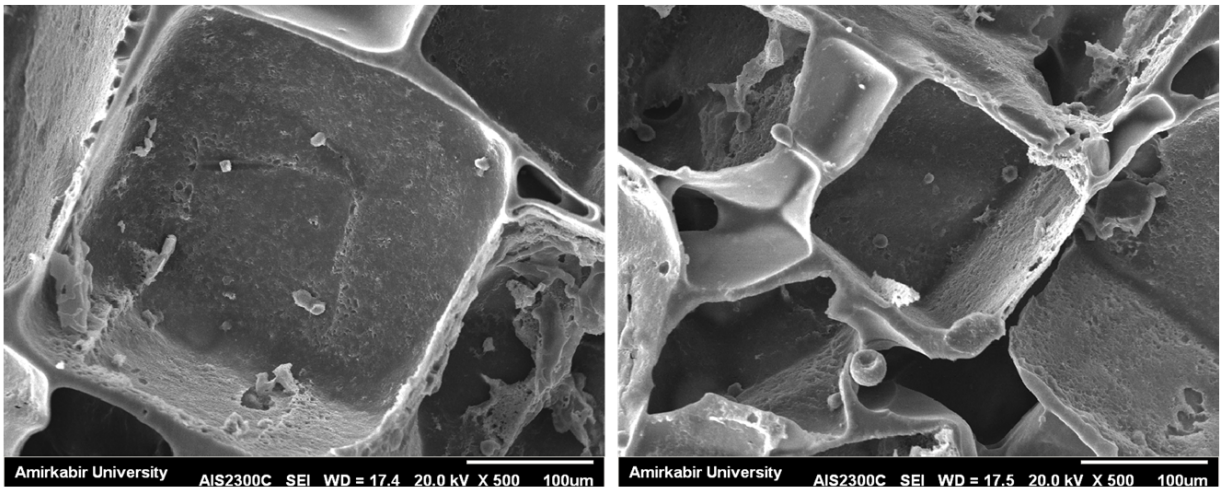

Figure 9. SEM micrographs of SH-SY5Y cells cultured on (left) S1 and (right) S4 scaffolds after 24 hours.

higher density of evenly distributed nuclei across all fields. The increased number of adherent cells is indicative of improved cell–substrate interactions, which may result from the synergistic effects of PCL incorporation and the presence of PPy- CNFs [49]. The nanofibrous architecture introduced by CNFs enhances surface roughness and wettability, favoring protein adsorption and integrin-mediated adhesion. Furthermore, the polypyrrole coating introduces mild electrical conductivity, which can activate calcium-mediated signaling pathways in neural cells, promoting adhesion, cytoskeletal arrangement, and even early neural differentiation [62]. The presence of hydrophilic functional groups (–OH, –NH, and –C=O) on the nanofiber-modified surface may also enhance electrostatic interactions with serum proteins such as fibronectin and laminin, further improving cellular affinity [63].

Moreover, the improved porous structure and water retention capacity in S4 likely contribute to better nutrient diffusion and a stable hydration environment around the seeded cells, supporting sustained viability and adhesion [64]. These microenvironmental enhancements explain the greater cellular density and uniformity observed in S4.

In addition, quantitative analysis of nuclear density was performed using ImageJ by counting DAPI-stained nuclei per mm^2. As shown in Fig. 10 (b), scaffold S4 exhibited a higher number of adhered nuclei compared to S1, consistent with qualitative fluorescence observations. Although the difference was not statistically significant ($p > 0.05$), the numerical trend supports the superior biointerface performance of the nanocomposite scaffold.

In addition to the observed cytocompatibility, the incorporation of polypyrrole-functionalized carbon nanofibers plays a key role in enhancing the suitability of the scaffolds for neural regeneration. Polypyrrole is an electroactive polymer, and its incorporation introduces electroactive domains within the scaffold that are compatible with the electrically responsive nature of neural tissue. Although external electrical stimulation was not applied in the present study, the presence of PPy can facilitate charge transfer at the cell–material interface, which has been reported to support neural cell adhesion and neurite-related cellular responses. Furthermore, the PPy-CNFs increase surface roughness and mechanical stability, both of which are critical parameters influencing neural cell attachment, survival, and morphology. Together, these features suggest that the PPy-functionalized scaffolds provide a multifunctional microenvironment favorable for neural regeneration [65, 7].

Overall, the observed cytocompatibility of the scaffolds is supported not only by the high cell viability values obtained from the MTT assay, but also by their favorable structural, surface, and mechanical characteristics. The interconnected porous architecture facilitates nutrient diffusion and waste removal, while the surface roughness induced by PPy-functionalized CNFs provides additional anchoring sites for cell attachment. Moreover, the improved mechanical integrity of the PGS/PCL/PPy-CNFs scaffolds helps preserve structural stability during cell culture, thereby reducing mechanical stress on adherent cells. Together, these features create a supportive microenvironment that promotes cell adhesion, survival, and proliferation.

Compared with many existing neural tissue engineering scaffolds, which often prioritize either mechanical compliance or electrical/biofunctional properties alone, the present PGS/PCL/PPy-CNFs system was designed to achieve a balanced integration of structural stability, elasticity, and bioactive surface features. Soft hydrogel-based scaffolds typically provide favorable cell compatibility but may lack sufficient mechanical robustness for handling and long-term structural maintenance, whereas rigid polymeric systems can offer strength at the expense of flexibility and tissue-matching behavior [66, 67]. In this study, the combination of elastomeric PGS with semi-crystalline PCL created a mechanically reinforced yet compliant matrix, while the incorporation of PPy-functionalized cellulose nanofibers introduced nanoscale reinforcement and surface modulation that supported improved cellular interaction. The progressive enhancement in mechanical response and cell viability observed

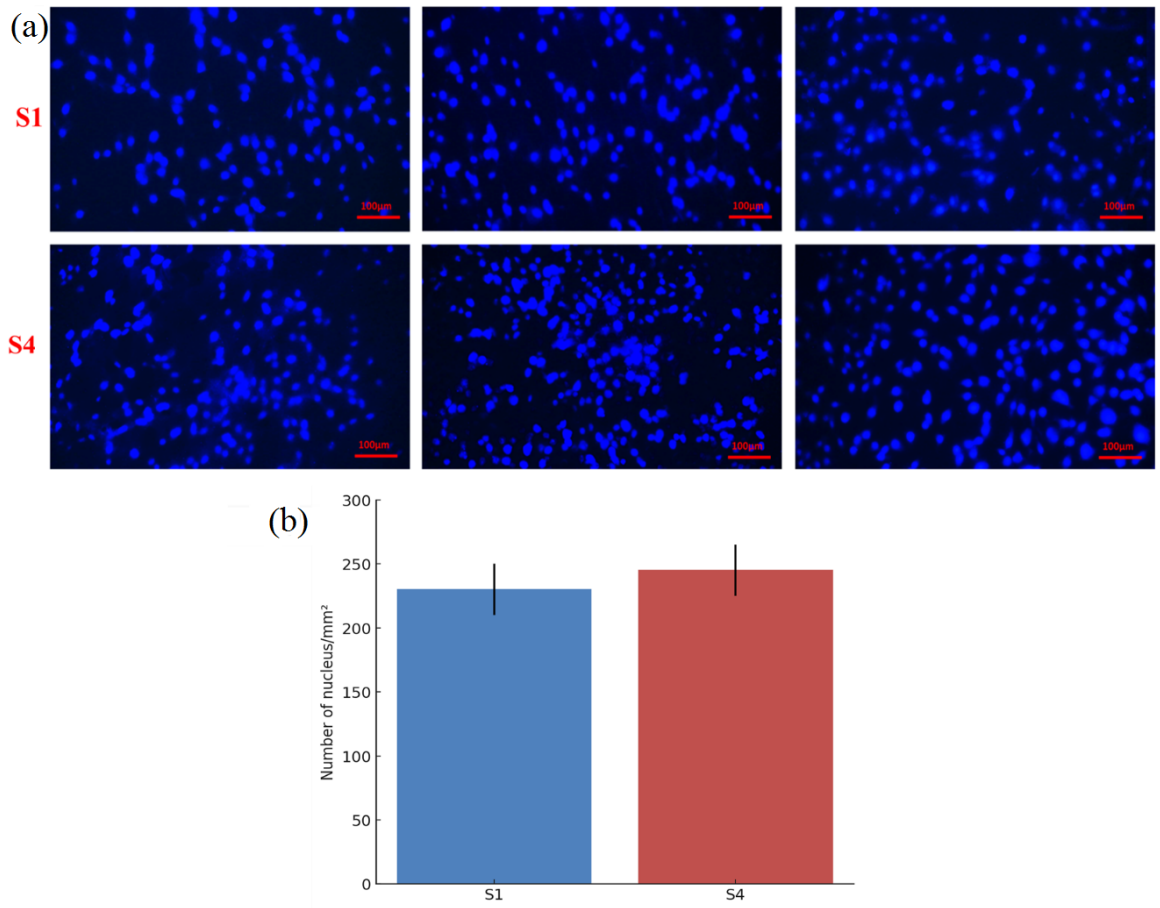

Figure 10. (a) Representative DAPI-stained fluorescence images of nuclei in SH-SY5Y cells cultured on, (b) Quantitative analysis of cell nuclei density (number of nucleus/mm^2) on S1 and S4 scaffolds. Results indicate a slightly higher number of adhered cells on S4 compared to S1. Data are presented as mean ± standard deviation (n = 3).

from S1 to S4 suggests that the hybrid reinforcement strategy provides a synergistic effect rather than a single-property improvement. Therefore, this scaffold design represents a complementary approach within neural tissue engineering strategies by simultaneously addressing mechanical integrity, structural cohesion, and biological performance within a unified platform.

4. Future perpective and conclusion

4.1 Future perpective

Although the developed PGS/PCL/PPy-CNF scaffolds demonstrated promising structural, electrical, and biological characteristics for neural tissue engineering, several limitations warrant further investigation. First, the current study was limited to short-term *in vitro* evaluation using a single neuronal cell line (SH-SY5Y), which may not fully reflect the complexity of *in vivo* neural environments. Future work should involve primary neuronal cells and extended culture durations to assess long-term biocompatibility, degradation behavior, and functionality. Second, while electrical conductivity was enhanced via PPy-CNFs incorporation, no external electrical stimulation was applied. Incorporating physiologically relevant electrical cues could potentially promote axonal alignment, neural differentiation, and synaptogenesis. Third, only two CNF concentrations (0.5% and 1%) were investigated; systematic variation of nanofiber content could further optimize scaffold performance. Moreover, *in vivo* studies using animal models of nerve injury are essential to evaluate immunological responses, integration with host tissues, and functional recovery outcomes. Finally, incorporating biochemical signaling molecules (e.g., neurotrophic factors or peptides) or integrating microfluidic channels may enable the development of next-generation scaffolds capable of mimicking the dynamic neural microenvironment. Collectively, these directions will facilitate the clinical translation of conductive, multifunctional nanocomposite scaffolds in regenerative neuroengineering.

4.2 Conclusion

A comprehensive evaluation of PGS-based scaffolds modified with PCL and PPy- CNFs demonstrated significant improvements in structural, mechanical, thermal, and biological properties, highlighting their suitability for neural tissue engineering.

Chemical characterization via FTIR confirmed the presence of characteristic ester bonds (C=O at 1735 cm^{-1}) and O–H groups, indicating successful crosslinking in PGS and effective blending with PCL. The incorporation of CNFs introduced additional peaks associated

https://doi.org/10.57647/pibm.2026.152606

with PPy and cellulose, confirming functionalization. XRD analysis revealed a shift from the amorphous profile of neat PGS to increased crystallinity in PGS/PCL and further in PGS/PCL/PPy- CNFs scaffolds, evidenced by sharper peaks near $2\theta = 21° - 24°$, reflecting enhanced structural order and mechanical stability.

Thermal analysis (TGA/DTG) showed that the pure PGS scaffold (S1) underwent degradation starting around 280 °C with a main DTG peak at 405 °C, indicating single-phase decomposition. In contrast, S2 (with PCL) displayed a two-step degradation profile with DTG peaks at 335 °C and 410 °C, attributed to PCL and PGS segments, respectively. S3 and S4, reinforced with 0.5% and 1% CNF, exhibited further thermal improvement, with DTG peaks at 345 °C and 425 °C and increased residual char at 500 °C, confirming enhanced thermal barrier effects of PPy-CNFs.

Mechanical properties improved significantly upon material modification. The Young's modulus increased from 1.8 MPa in S1 to 5.7 MPa in S4, and compressive strength rose from 7 MPa (S1) to 24 MPa (S4). These enhancements are attributed to the reinforcing effect of PCL and CNFs, which increase matrix stiffness and load-bearing capacity while reducing deformation under compressive stress.

Wettability analysis indicated a consistent decrease in contact angle from 62° in S1 to 71.8° in S4, suggesting increased hydrophobicity due to PPy presence, yet remaining within a range compatible with neural cell attachment and viability.

Biocompatibility, assessed through MTT assay on SH-SY5Y cells, confirmed that all scaffolds-maintained cell viability above the ISO threshold of 70%. Cell viability increased progressively from 84.94% in S1 to 91.09% in S4, demonstrating the positive impact of PCL and especially CNFs on cell health. The highest viability in S4 is attributed to improved surface bioactivity, moderate conductivity from PPy, and nanoscale topography favoring cytoskeletal anchoring.

Cell adhesion and spreading assays revealed superior cell–scaffold interaction in nanofiber-loaded samples, especially S4, where well-distributed filopodia and cytoplasmic extensions were observed. This indicates the synergistic role of physical cues (surface roughness), chemical signals (PPy), and mechanical properties in promoting neural cell compatibility.

In conclusion, the integration of PCL and PPy-CNFs into PGS scaffolds markedly enhanced their performance across all critical parameters. Among the tested formulations, S4 (PGS70/PCL30/1%PPy- CNFs) emerged as the optimal scaffold, exhibiting the highest mechanical strength, thermal stability, cell viability, and biointerface activity, making it a promising candidate for advanced neural tissue engineering applications.

Authors contributions
All authors contributed equally to the conception, design, execution, and writing of this work. All authors read and approved the final manuscript.

Availability of data and materials
The datasets generated during and/or analyzed during the current study are available from the corresponding author on reasonable request.

Conflict of interests
The authors declare that they have no known competing financial interests or personal relationships that could have appeared to influence the work reported in this paper.

References

1. Huang WH et al. Collagen for neural tissue engineering: Materials, strategies, and challenges. Mater. Today Bio. 2023; 20. DOI: 10.1016/J.MTBIO.2023.100639
2. Patel JC, Shukla M, and Shukla M. Cellular and molecular interactions in CNS injury: The role of Immune cells and inflammatory responses in damage and repair. Cells 2025; 14:918. DOI: 10.3390/cells14120918
3. Afshari M, Pourmadadi M, Shabestari SM, Abdouss H, and Abdouss M. Development and characterization of biocompatible Gelatin/Polyethylene Glycol/Copper-Doped carbon quantum Dots@Curcumin nanocarriers for pH-Sensitive curcumin delivery in glioblastoma treatment. Inorg. Chem. Commun. 2025; 179:114782. DOI: 10.1016/J.INOCHE.2025.114782
4. Wang Y, Zhang Y, Li X, and Zhang Q. The progress of biomaterials in peripheral nerve repair and regeneration. J. Neurorestoratology 2020; 8:252–269. DOI: 10.26599/JNR.2020.9040022
5. Chen Z et al. Progress in biomaterials inspired by the extracellular matrix. Giant 2024; 19:100323. DOI: 10.1016/j.giant.2024.100323
6. Song S, Li C, Xiao Y, Ye Z, Rong M, and Zeng J. Beyond conventional therapies: MSCs in the battle against nerve injury. Regen. Ther. 2025; 28:280–291. DOI: 10.1016/j.reth.2024.12.017
7. Rahmatipour H, Shabestari SM, Benisi SZ, and Samadikhah H. Pioneering pain management with botulinum toxin type A: From anti-inflammation to regenerative therapies. Heliyon 2025; 11:e42350. DOI: 10.1016/j.heliyon.2025.e42350
8. Qian Y, Lin H, Yan Z, Shi J, and Fan C. Functional nanomaterials in peripheral nerve regeneration: Scaffold design, chemical principles and microenvironmental remodeling. Mater. Today 2021; 51:165–187. DOI: 10.1016/j.mattod.2021.09.014

9. Shomali H, Rahmatipour H, Benisi SZ, Shabestari M, and Mahmoudifard M. Graphene oxide and quantum dot-enhanced alginate Scaffolds: Structural, mechanical, and biological correlations for neural tissue engineering applications. Acta Biochim Biophys Sin (Shanghai) 2025; 14
10. Liu YY and Echeverry-Rendón M. 3D-printed biodegradable polymer scaffolds for tissue engineering: An overview, current stage and future perspectives. Next Mater. 2025; 8. DOI: 10.1016/j.nxmate.2025.100647
11. Manivannan RK, Sharma N, Kumar V, Jayaraj I, Vimal S, and Umesh M. A comprehensive review on natural macromolecular biopolymers for biomedical applications: Recent advancements, current challenges, and future outlooks. Carbohydr. Polym. Technol. Appl. 2024; 8:100536. DOI: 10.1016/J.CARPTA.2024.100536
12. Suamte L, Tirkey A, and Babu PJ. Design of 3D smart scaffolds using natural, synthetic and hybrid derived polymers for skin regenerative applications. Smart Materials in Medicine 2023; 4:243–256. DOI: 10.1016/j.smaim.2022.09.005
13. Pourmadadi M et al. Green Synthesis of pH-Sensitive Carboxymethyl Cellulose/Agarose/Carbon Quantum Dots Nanocarriers for Quercetin Delivery to A549 Lung Cancer Using an Emulsification Method. Bionanoscience 2024 :1–15. DOI: 10.1007/s12668-024-01426-9
14. Talouki PY et al. Progress in Biomaterials (PIBM) Controlling Hydroxyapatite Ratio in Poly (glycerol sebacate)/Polycaprolactone/Chitosan Scaffolds Directs Chondrogenesis of Adipose-Derived Mesenchymal Stem Cells for Cartilage Regeneration. 2024; 13:1–19
15. Asgharnejad-laskoukalayeh M et al. Preparation and characterization of a new sustainable bio-based elastomer nanocomposites containing poly(glycerol sebacate citrate)/chitosan/n-hydroxyapatite for promising tissue engineering applications. J. Biomater. Sci. Polym. Ed. 2022; 33:2385–2405. DOI: 10.1080/09205063.2022.2104600
16. Godinho B, Nogueira R, Gama N, and Ferreira A. Synthesis and Characterization of Poly(glycerol sebacate), Poly(glycerol succinate) and Poly(glycerol sebacate-co-succinate). J. Polym. Environ. 2024. DOI: 10.1007/s10924-024-03212-w
17. Shabestari SM et al. Role of phosphate-modified cellulose into the scaffold based on poly (glycerol azelaic acid)-co-poly(ε-caprolactone) for using bone regenerative medicine. Int. J. Biol. Macromol. 2025; 304:140855. DOI: 10.1016/j.ijbiomac.2025.140855
18. Ebrahimi Z, Irani S, Ardeshirylajimi A, and Seyedjafari E. Enhanced osteogenic differentiation of stem cells by 3D printed PCL scaffolds coated with collagen and hydroxyapatite. Sci. Rep. 2022 :1–15. DOI: 10.1038/s41598-022-15602-y
19. Rostamian M, Kalaee MR, Dehkordi SR, Panahi-Sarmad M, Tirgar M, and Goodarzi V. Design and characterization of poly(glycerol-sebacate)-co-poly(caprolactone) (PGS-co-PCL) and its nanocomposites as novel biomaterials: The promising candidate for soft tissue engineering. Eur. Polym. J. 2020; 138:109985. DOI: 10.1016/J.EURPOLYMJ.2020.109985
20. Shlapakova LE, Surmeneva MA, Kholkin AL, and Surmenev A. Materials Today Bio Revealing an important role of piezoelectric polymers in nervous-tissue regeneration: A review. Mater. Today Bio 2024; 25:100950. DOI: 10.1016/j.mtbio.2024.100950
21. Ranjbar N and Bakhshandeh B. Electroconductive Nanofibrous Scaffolds Enable Neuronal Differentiation in Response to Electrical Stimulation without Exogenous Inducing Factors. 2023
22. Liang Y and Goh JCH. Polypyrrole-Incorporated Conducting Constructs for Tissue Engineering Applications: A Review. Bioelectricity 2020; 2:101. DOI: 10.1089/BIOE.2020.0010
23. Hao L, Yu D, Hou X, and Zhao Y. Advances in Polypyrrole Nanofiber Composites: Design, Synthesis, and Performance in Tissue Engineering. Materials (Basel) 2025; 18:2965. DOI: 10.3390/ma18132965
24. Jose SA et al. A Comprehensive Review on Cellulose Nanofibers, Nanomaterials, and Composites: Manufacturing, Properties, and Applications. Nanomaterials 2025; 15:1–33. DOI: 10.3390/nano15050356
25. Turnbull G et al. 3D bioactive composite scaffolds for bone tissue engineering. Bioactive Materials 2018; 3:278–314. DOI: 10.1016/j.bioactmat.2017.10.001
26. Hases L, Archer A, and Williams C. ERβ and Inflammation. Advances in Experimental Medicine and Biology 2022; 1390:213–225. DOI: 10.1007/978-3-031-11836-4_12
27. Muzzio N, Moya S, and Romero G. Multifunctional scaffolds and synergistic strategies in tissue engineering and regenerative medicine. Pharmaceutics 2021; 13. DOI: 10.3390/pharmaceutics13060792
28. Tamo AK. Nanocellulose-based hydrogels as versatile materials with interesting functional properties for tissue engineering applications. Journal of Materials Chemistry B 2024; 12:7692–7759. DOI: 10.1039/d4tb00397g
29. Shabestari SM et al. pH-responsive chitosan-sodium alginate nanocarriers for curcumin delivery against brain cancer. Colloids Surfaces B Biointerfaces 2025; 225. DOI: 10.1016/j.colsurfb.2025.114875

30. Pourmadadi M et al. Development of Poly(ether sulfone)/Poly(vinyl alcohol)/Magnesium-Doped Carbon Quantum Dot Scaffolds for Bone Tissue Engineering. ACS Biomater. Sci. Eng. 2025. DOI: 10.1021/acsbiomaterials.4c02124

31. Pourmadadi M, Fallahi F, Alesheikh M, and Mohammadi S. In vitro evaluation of bioinspired PEC/Zein/ZnO nanocarriers for pH-responsive curcumin delivery in colorectal cancer therapy. Carbohydr. Polym. Technol. Appl. 2025; 12. DOI: 10.1016/j.carpta.2025.101044

32. Naseripour M, Ahmadi T, Shojaei S, Shabestari SM, and Goodarzi V. Preparation and Assessment of Polyurethane-Polygycerol Itaconate-ZnO Composite as Guided Bone Regeneration Scaffold. 2025; 14

33. Ahmed RA, Rashid S, and Huddersman K. Esterification of stearic acid using novel protonated and crosslinked amidoximated polyacrylonitrile ion exchange fibres. J. Ind. Eng. Chem. 2023; 119:550–573. DOI: 10.1016/J.JIEC.2022.12.001

34. Sood Y et al. Heliyon Insights into properties, synthesis and emerging applications of polypyrrole-based composites, and future prospective: A review. Heliyon 2024; 10:e33643. DOI: 10.1016/j.heliyon.2024.e33643

35. Goncalves D. Preparation and characterization of cellulose paper/polypyrrole/bromophenol blue composites for disposable optical sensors. Open Chem. 2016; 14:404–411. DOI: 10.1515/chem-2016-0043

36. Salehi S, Bahners T, Gutmann JS, Gao SL, Mäder E, and Fuchsluger TA. Characterization of structural, mechanical and nano-mechanical properties of electrospun PGS/PCL fibers. RSC Adv. 2014; 4:16951–16957. DOI: 10.1039/C4RA01237B

37. Chen XB et al. Bioactive Materials Biomaterials/bioinks and extrusion bioprinting. Bioact. Mater. 2023; 28:511–536. DOI: 10.1016/j.bioactmat.2023.06.006

38. Khatti T, Naderi-Manesh H, and Kalantar SM. Polypyrrole-Coated Polycaprolactone-Gelatin Conductive Nanofibers: Fabrication and Characterization. Mater. Sci. Eng. B 2019; 250:114440. DOI: 10.1016/J.MSEB.2019.114440

39. Selim M et al. Fabrication and characterization of a highly degradable 3D-printed composite scaffold. Mater. Today Commun. 2025; 46:112764. DOI: 10.1016/J.MTCOMM.2025.112764

40. Ntrivala MA et al. Polycaprolactone (PCL): the biodegradable polyester shaping the future of materials – a review on synthesis, properties, biodegradation, applications and future perspectives. 2025; European Polymer Journal. DOI: 10.1016/j.eurpolymj.2025.114033

41. Zahedifar P, Morent R, Aliakbarshirazi S, Ghobeira R, and Geyter ND. Enhancement of the Bio-Responsiveness of PCL Nanofibers via the Combination of a Thiol Plasma-Polymerized Coating and Fibronectin Immobilization. Appl. Surf. Sci. Adv. 2025; 27. DOI: 10.1016/j.apsadv.2025.100752

42. Rusu AG, Popa MI, Lisa G, and Vereştiuc L. Thermal behavior of hydrophobically modified hydrogels using TGA/FTIR/MS analysis technique. Thermochim. Acta 2015; 613:28–40. DOI: 10.1016/J.TCA.2015.05.018

43. Larranaga A and Lizundia E. A review on the thermomechanical properties and biodegradation behaviour of polyesters. Eur. Polym. J. 2019; 121:109296. DOI: 10.1016/J.EURPOLYMJ.2019.109296

44. Zhou TY, Tsui GCP, Liang JZ, Zou SY, Tang CY, and Mišković-Stanković V. Thermal properties and thermal stability of PP/MWCNT composites. Compos. Part B Eng. 2016; 90:107–114. DOI: 10.1016/J.COMPOSITESB.2015.12.013

45. Xu B, Li Y, Zhu C, Cook WD, Forsythe J, and Chen Q. Fabrication, mechanical properties and cytocompatibility of elastomeric nanofibrous mats of poly(glycerol sebacate). Eur. Polym. J. 2015; 64:79–92. DOI: 10.1016/J.EURPOLYMJ.2014.12.008

46. Cai Y et al. The Improvement of Thermal Stability and Conductivity via Incorporation of Carbon Nanofibers into Electrospun Ultrafine Composite Fibers of Lauric Acid/Polyamide 6 Phase Change Materials for Thermal Energy Storage. Int. J. Green Energy 2014; 11:861–875. DOI: 10.1080/15435075.2013.829068

47. Vishnu S, Prabu B, and Pugazhvadivu M. Strategies to improve the mechanical performance of elastomers using ternary blends: A review. Hybrid Adv. 2023; 3:100062. DOI: 10.1016/j.hybadv.2023.100062

48. Zhang H, Luo X, Lin X, Lu X, Zhou Y, and Tang Y. Polycaprolactone/chitosan blends: Simulation and experimental design. Mater. Des. 2016; 90:396–402. DOI: 10.1016/J.MATDES.2015.10.108

49. Parit M, Du H, Zhang X, Prather C, Adams M, and Jiang Z. Polypyrrole and cellulose nanofiber based composite films with improved physical and electrical properties for electromagnetic shielding applications. Carbohydr. Polym. 2020; 240:116304. DOI: 10.1016/J.CARBPOL.2020.116304

50. Adabavazeh Z, Johari N, and Baino F. Electrospun conductive polymer scaffolds: Tailoring fiber diameter and electrical properties for tissue engineering applications. Mater. Today Commun. 2025; 46:112596. DOI: 10.1016/j.mtcomm.2025.112596

51. Mohammed M et al. Surface treatment to improve water repellence and compatibility of natural fiber with polymer matrix: Recent advancement. Polym. Test. 2022; 115:107707. DOI: 10.1016/j.polymertesting.2022.107707

52. Eryildiz M, Karakus A, Demirci M, Kadirhan OA, and Altan ME. Optimization of Thermal, Mechanical, Biodegradation, and Shape Memory Properties in 4D-Printed PLA/PCL Blends for Spinal Cages. Polym. Adv. Technol. 2025; 36:e70133. DOI: 10.1002/PAT.70133

53. Kayan GO and Kayan A. Polycaprolactone Composites/Blends and Their Applications Especially in Water Treatment. ChemEngineering 2023; 7:104. DOI: 10.3390/CHEMENGINEERING7060104

54. Forsberg P, Nikolajeff F, and Karlsson M. Cassie–Wenzel and Wenzel–Cassie transitions on immersed superhydrophobic surfaces under hydrostatic pressure. Soft Matter 2010; 7:104–109. DOI: 10.1039/C0SM00595A

55. Oesef K, Cranston ED, and Abdin Y. Current advances in processing and modification of cellulose nanofibrils for high-performance composite applications. Mater. Des. 2024; 247:113417. DOI: 10.1016/J.MATDES.2024.113417

56. Gultekinoglu M, Öztürk S, Chen B, Edirisinghe M, and Ulubayram K. Preparation of poly(glycerol sebacate) fibers for tissue engineering applications. Eur. Polym. J. 2019; 121:109297. DOI: 10.1016/J.EURPOLYMJ.2019.109297

57. Borhan S, Hesaraki S, and Shahrezaee M. Evaluation of 3D printed polycaprolactone/tetracalcium phosphate nanocomposite as potential scaffold for bone tissue engineering. J. Mater. Res. Technol. 2025; 36:1130–1145. DOI: 10.1016/J.JMRT.2025.03.098

58. Luo S et al. Advances in electroactive biomaterials: Through the lens of electrical stimulation promoting bone regeneration strategy. Journal of Orthopaedic Translation 2024; 47:191–206. DOI: 10.1016/j.jot.2024.06.009

59. Nasser RA, Arya SS, Alshehhi KH, Teo JCM, and Pitsalidis C. Conducting polymer scaffolds: A new frontier in bioelectronics and bioengineering. Trends Biotechnol. 2024; 42:760–779. DOI: 10.1016/J.TIBTECH.2023.11.017

60. Sundback CA et al. Biocompatibility analysis of poly(glycerol sebacate) as a nerve guide material. Biomaterials 2005; 26:5454–5464. DOI: 10.1016/J.BIOMATERIALS.2005.02.004

61. Abedi S, Mohajeri A, Benisi SZ, Pezeshki-Modaress M, and Shabestari SM. Three-dimensional nanofibrous PCL/gelatin scaffold fabricated using centrifugal force assisted wet electrospinning technique. Sci. Rep. 2025; 15:1–24. DOI: 10.1038/s41598-025-20814-z

62. Balint R, Cassidy NJ, and Cartmell SH. Conductive polymers: Towards a smart biomaterial for tissue engineering. Acta Biomater. 2014; 10:2341–2353. DOI: 10.1016/J.ACTBIO.2014.02.015

63. Niemczyk-Soczynska B, Gradys A, and Sajkiewicz P. Hydrophilic Surface Functionalization of Electrospun Nanofibrous Scaffolds in Tissue Engineering. Polymers (Basel) 2020; 12:2636. DOI: 10.3390/polym12112636

64. Zhu S et al. 3D bioprinting of high-performance hydrogel with in-situ birth of stem cell spheroids. Bioact. Mater. 2025; 43:392–405. DOI: 10.1016/J.BIOACTMAT.2024.09.033

65. Tavakoli AM, Tarasi R, Sedghi R, and Moghimi A. Fabrication of nanochitosan incorporated polypyrrole/alginate conducting scaffold for neural tissue engineering. Sci. Rep. 2020 :1–10. DOI: 10.1038/s41598-020-78650-2

66. Peressotti S, Koehl GE, Goding JA, and Green RA. Self-Assembling Hydrogel Structures for Neural Tissue Repair. ACS Biomaterials Science and Engineering 2021; 7:4136–4163. DOI: 10.1021/acsbiomaterials.1c00030

67. Shabestari SM et al. Unlocking the potential of cytarabine: A comprehensive review from molecular insights to advanced nanoformulations and Co-delivery strategies for enhanced drug efficacy. J. Drug Deliv. Sci. Technol. 2024; 102:106346. DOI: 10.1016/J.JDDST.2024.106346